J. Fluid Mech. (1996), *vol.* 316, *pp.* 173–196

An analysis of aerodynamic forces on a delta wing

By CHIEN-CHENG CHANG AND SHENG-YUAN LEI

Institute of Applied Mechanics, College of Engineering, National Taiwan University, Taipei 10764, Taiwan, Republic of China

(Received 13 June 1994 and in revised form 19 January 1996)

The present study aims at relating lift and drag to flow structures around a delta wing of elliptic section. Aerodynamic forces are analysed in terms of fluid elements of non-zero vorticity and density gradient. The flow regime considered is $M_\infty = 0.6 \sim 1.8$ and $\alpha = 5° \sim 19°$, where M_∞ denotes the free-stream Mach number and α the angle of attack. Let ρ denote the density, $\boldsymbol{u}$ velocity, and $\boldsymbol{\omega}$ vorticity. It is found that there are two major source elements $R_e(\boldsymbol{x})$ and $V_e(\boldsymbol{x})$ which contribute about 95% or even more to the aerodynamic forces for all the cases under consideration,

$$R_e(\boldsymbol{x}) = -\tfrac{1}{2}\boldsymbol{u}^2\nabla\rho\cdot\nabla\phi \quad \text{and} \quad V_e(\boldsymbol{x}) = -\rho\boldsymbol{u}\times\boldsymbol{\omega}\cdot\nabla\phi,$$

where ϕ is an acyclic potential, generated by the delta wing moving with unit velocity in the negative direction of the force (lift or drag). All the physical quantities are non-dimensionalized. Detailed force contributions are analysed in terms of the flow structures and the elements $R_e(\boldsymbol{x})$ and $V_e(\boldsymbol{x})$. The source elements $R_e(\boldsymbol{x})$ and $V_e(\boldsymbol{x})$ are concentrated in the following regions: the boundary layer in front of (below) the delta wing, the primary and secondary vortices over the delta wing, and a region of expansion around the leading edge. It is shown that $V_e(\boldsymbol{x})$ due to vorticity prevails as the source of forces at relatively low Mach number, $M_\infty < 0.7$. Above about $M_\infty = 0.75$, $R_e(\boldsymbol{x})$ due to compressibility generally becomes the dominating contributor to the lift, while the overall contribution from $V_e(\boldsymbol{x})$ decreases with increasing M_∞, and even becomes negative at $M_\infty = 1.2$ for the lift, and at a higher M_∞ for the drag. The analysis is carried out with the aid of detailed numerical results by solving the Reynolds-averaged Navier–Stokes equations, which are in close agreement with experiments in comparisons of the surface pressure distributions.

1. Introduction

Aerodynamic forces generated by vortex systems have been of great interest during past several decades. This is true for flows around finite bodies in a wide range of flow conditions from low subsonic to high Mach number flows. In the literature, extensive study of such flows has extended from geometrically simple bodies to rather practical profiles. Among them, delta wings are efficient wing profiles for flight vehicles at high speeds of cruise, and are renowned for their vortex systems at angles of attack. The vortex systems are considered to be the major source of lift (and also drag). The present study aims therefore at investigating how individual flow structures contribute to the aerodynamic forces through their vorticity and compressibility. It is not fully understood as yet which parts of and how a vortex system contributes to

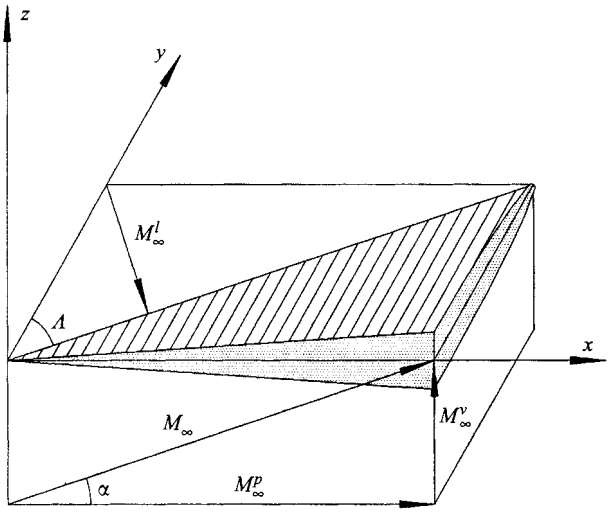

FIGURE 1. Geometric definitions of the physical problem.

the aerodynamic forces and as far as the aerodynamic forces are concerned, whether there are other flow structures of comparable importance, and how vorticity and compressibility interplay to make different contributions to the aerodynamic forces under different free-stream Mach numbers M_∞ and angles of attack α.

The highly swept profile of a delta wing facilitates the generation of vortex systems due to leading-edge separation. Previous works on flows over a delta wing of various profiles cover a wide range of Mach numbers and angles of attack. Since the vorticity may be considered the only source of aerodynamic forces at low Mach numbers, there is no doubt that the vortex systems over a delta wing contribute to the lift and drag through their vorticity. However, the term 'vortex' includes not only the meaning of vorticity but also compressibility at high Mach numbers. There have been several formulations which allow us to view the vorticity as a source of aerodynamic forces; see e.g. Lighthill (1986, p. 214), Phillips (1956) and Wu (1981). The viewpoints are however limited to incompressible flows with constant densities and viscosities. In order to take into account the effect of compressibility, we need to have a consistent theory, which can be extended to viscous compressible flows. The recent force theory proposed by Chang (1992) for incompressible viscous flows is here extended to analyse aerodynamic forces on a delta wing. The surface pressure force is decomposed by introducing an auxiliary potential ϕ^* (or ϕ) to several volume and surface integrals; each integrand of them will be termed a source element, which is related to either vorticity or compressibility such as dilatation or density gradient. All the source elements of the volume integrals decay rapidly away from the body. This decomposition enables us to analyse the aerodynamic forces in terms of vorticity and compressibility, which is in strong contrast to the conventional analysis based on the surface pressure distribution, which cannot differentiate contributions of individual flow structures nor contributions due to vorticity and those due to compressibility.

Figure 1 shows the geometric definitions of the present delta wing with a swept angle $\Lambda = 70°$. The delta wing is of elliptic section with axis ratio 14 : 1 at an angle of attack from $\alpha = 5°$ to 19° to a constant stream of Mach number M_∞ between 0.6 and 1.8. This choice enables us to validate numerical results by comparison with the experimental results of Squire (1985). Squire's experimental results indicate, in

particular, that we may also safely assume, for the flow regime considered, the flow to be steady without occurrence of vortex breakdown. With α, Λ and M_∞, we may define

$$M_\infty^v = M_\infty \sin\alpha, \quad M_\infty^p = M_\infty \cos\alpha, \quad M_\infty^l = M_\infty^p \cos\Lambda,$$

where M_∞^v denotes the component normal to the wing's planform, M_∞^p denotes the parallel component, while M_∞^l denotes the component normal to the leading edge on the plane of the planform. Note however that the most extensively studied profiles are sharp-edged delta wings, for which flow patterns were well classified by Miller & Wood (1983) following the earlier work of Stanbrook & Squire (1964), and were somewhat modified by McMillin, Pittman & Thomas (1990) in a wide range of flow conditions based on the parameters $M_\infty^N = (M_\infty^{v2} + M_\infty^{l2})^{1/2}$ and $\alpha_N = \tan^{-1}(M_\infty^v/M_\infty^l)$. Moreover, for M_∞ from 0 to 0.8, Schrader, Reynolds & Novak (1988) have shown that the lift coefficient decreases with increasing the Mach number M_∞, and the strength of the vortex system increases more rapidly with increasing the angle of attack at relatively lower Mach number. The main purpose of the study is to identify by numerical analysis the major source elements which contribute to the aerodynamic forces, and to discuss the physical significance of such an investigation. The idea underlined is that different source elements are not of the same significance: some elements are expected to be more important than others. The present analysis is particularly useful only when a few source elements are much more significant than others. The flow information is obtained by solving the Navier–Stokes equations in conservation form by a numerical method of TVD type, developed relatively recently by other authors. Newsome (1986) was able to show it inadequate to simply solve the inviscid Euler's equations, which could lead to physically incorrect solutions. To include the effect of turbulence, an isotropic algebraic two-layer eddy-viscosity turbulence model is incorporated in the formulation of the Reynolds-averaged Navier–Stokes equations.

2. Auxiliary acyclic potential flow

Consider a solid body moving through an incompressible fluid of constant density. The dimensional physical quantities are denoted with an asterisk '*'. Let us first determine the nature of the acyclic potential solution at great distances from the moving body. The potential function of the flow satisfies Laplace's equation, $\Delta^*\phi^* = 0$. The solution is required to vanish at infinity where the fluid is at rest. In three space dimensions, the general form of the solution at great distances is given by

$$\phi^* = (\boldsymbol{A}^* \cdot \nabla^*)\frac{1}{|\boldsymbol{x}^*|} + \cdots = -\frac{\boldsymbol{A}^* \cdot \hat{\boldsymbol{x}}}{|\boldsymbol{x}^*|^2} + \cdots, \tag{1}$$

and the velocity $\boldsymbol{v}_\phi^* = \nabla^*\phi^*$ is

$$\boldsymbol{v}_\phi^* = (\boldsymbol{A}^* \cdot \nabla^*)\nabla^*\frac{1}{|\boldsymbol{x}^*|} + \cdots = \frac{3(\boldsymbol{A}^* \cdot \hat{\boldsymbol{x}})\hat{\boldsymbol{x}} - \boldsymbol{A}^*}{|\boldsymbol{x}^*|^3} + \cdots, \tag{2}$$

where $\hat{\boldsymbol{x}}$ denotes the unit vector in the direction of $\boldsymbol{x}^*$. The vector $\boldsymbol{A}^*$ depends on the actual shape of the body and its motion, and can be determined only by solving the full potential equation $\Delta^*\phi^* = 0$ (Landau & Lifshitz 1987, p. 27). Given a Neumann condition on the body, it can be shown then that the acyclic potential is uniquely determined (cf. Vladimirov 1971, p. 311).

For later use, it should be kept in mind that the potential function decays rapidly to

0 as $|x^*|$ tends to infinity. Precisely speaking, in three space dimensions the potential function ϕ^* decays at a rate of $O(1/|x^*|^2)$, and the corresponding velocity v_ϕ^* decays at a rate of $O(1/|x^*|^3)$. These rapidly convergent properties enter the source elements to be proposed in the next section, and thus distinguish the present analysis of aerodynamic forces from early approaches by other authors.

3. A finite body in a constant stream

Consider a finite body moving with a constant velocitythrough a viscous compressible fluid which is otherwise of uniform properties and at rest. Let ρ^* denote the density, v^* the velocity, and P^* the pressure; the flow is assumed to be governed by the Navier–Stokes equations (cf. White 1991, p. 68)

$$\rho^* \frac{Dv_i^*}{Dt^*} = -\frac{\partial P^*}{\partial x_i^*} + \frac{\partial \tau_{ij}^*}{\partial x_j^*}, \tag{3}$$

where $\tau_{ij}^* = \lambda^* \vartheta^* \delta_{ij} + 2\mu^* E_{ij}^*$ is the viscous stress tensor, and μ^* and λ^* denote respectively the first and second viscosities. Abbreviated notation is adopted in equation (3); we have the dilatation $\vartheta^* = \partial v_j^*/\partial x_j^*$ and the deformation tensor $2E_{ij}^* = \partial v_i^*/\partial x_j^* + \partial v_j^*/\partial x_i^*$. Let S_0^* denote the surface of the body; the most commonly used force formula is given by the sum of the force due to pressure and that due to friction

$$\int_{S_0^*} P^* n_i \, dA^* - \int_{S_0^*} \tau_{ij}^* n_j \, dA^*, \tag{4}$$

where n_i denotes the unit vector directed toward the inside of the body. The body is assumed to move with a constant velocity c^* in a certain direction. For a frame moving with the body, equation (3) can be rewritten, with $v^* = c^* + u^*$, as

$$-\frac{\partial P^*}{\partial x_i^*} = \rho^* \left(\frac{\partial u_i^*}{\partial t^*} + u_j^* \frac{\partial u_i^*}{\partial x_j^*} \right) - \frac{\partial \tau_{ij}^*}{\partial x_j^*} \tag{5}$$

where we notice that τ_{ij}^* (ϑ^* and E_{ij}^*) may also be expressed in terms of u_i^* instead of v_i^*, and that for this frame the velocity on the body surface is 0.

Let V_R^* be the volume of fluid enclosed by S^* which consists of the body surface S_0^* and a spherical surface S_R^* of radius R. Taking inner products with $\nabla^* \phi^*$ on both sides of (5) within V_R^*, and then letting $R \to \infty$, leaving out all the surface integrals at $|x^*| = R$, yields various terms which will be considered below. First the left-hand side of (5) gives

$$-\int_{V^*} \frac{\partial P^*}{\partial x_j^*} \frac{\partial \phi^*}{\partial x_j^*} \, dV^* = -\int_{S_0^*} P^* \frac{\partial \phi^*}{\partial x_j^*} n_j \, dA^*. \tag{6}$$

For the unsteady term, we simply have

$$\int_{V^*} \rho^* \frac{\partial u^*}{\partial t^*} \cdot \nabla^* \phi^* \, dV^* = \int_{V^*} \rho^* \frac{\partial u_j^*}{\partial t^*} \frac{\partial \phi^*}{\partial x_j^*} \, dV^*, \tag{7}$$

while the nonlinear term gives the contribution

$$-\frac{1}{2} \int_{V^*} u^{*2} \frac{\partial \rho^*}{\partial x_j^*} \frac{\partial \phi^*}{\partial x_j^*} \, dV^* - \int_{V^*} \rho^* \epsilon_{ijk} \frac{\partial \phi^*}{\partial x_i^*} u_j^* \omega_k^* \, dV^*. \tag{8}$$

These expressions were derived by repeatedly using the fact that ϕ^* is a harmonic function and applying the divergence theorem. For the viscous terms, we notice that the last term on the right-hand side of (5) can be written

$$-\frac{\partial}{\partial x_i^*}(\lambda^*\vartheta^*) - 2\mu^*\frac{\partial \vartheta^*}{\partial x_i^*} + \mu^*\epsilon_{ijk}\frac{\partial \omega_k^*}{\partial x_j^*} - 2\frac{\partial \mu^*}{\partial x_j^*}E_{ij}^*. \tag{9}$$

The first two terms of (9) give

$$-\int_{S_0^*}\kappa^*\vartheta^*\frac{\partial \phi^*}{\partial x_j^*}n_j\,\mathrm{d}A^* + 2\int_{V^*}\vartheta^*\frac{\partial \mu^*}{\partial x_j^*}\frac{\partial \phi^*}{\partial x_j^*}\,\mathrm{d}V^*, \tag{10}$$

where for simplicity we set $\kappa^* = \lambda^* + 2\mu^*$, while, for the third term, we have the contribution

$$\int_{S_0^*}\mu^*\epsilon_{ijk}n_j\omega_k^*\frac{\partial \phi^*}{\partial x_i^*}\,\mathrm{d}A^* - \int_{V^*}\epsilon_{ijk}\frac{\partial \mu^*}{\partial x_i^*}\omega_j^*\frac{\partial \phi^*}{\partial x_k}\,\mathrm{d}V^*. \tag{11}$$

Finally, we have the contribution from the fourth term of (9),

$$-2\int_{V^*}\frac{\partial \mu^*}{\partial x_i^*}E_{ij}^*\frac{\partial \phi^*}{\partial x_j^*}\,\mathrm{d}V^*.$$

Now, of immediate importance is that some assumptions have to be made concerning leaving out the surface integrals at $|\boldsymbol{x}^*| = R$, as $R \to \infty$. These integrals are

$$\int_{S_R^*}P^*\frac{\partial \phi^*}{\partial n}\,\mathrm{d}A^*, \quad \int_{S_R^*}\frac{1}{2}\rho^*\boldsymbol{u}^{*2}\frac{\partial \phi^*}{\partial n}\,\mathrm{d}A^*, \tag{12a}$$

$$\int_{S_R^*}\kappa^*\vartheta^*\frac{\partial \phi^*}{\partial n}\,\mathrm{d}A^*, \quad \int_{S_R^*}\mu^*\epsilon_{ijk}n_j\omega_k^*\frac{\partial \phi^*}{\partial x_i^*}\,\mathrm{d}A^*. \tag{12b}$$

Notice that $\nabla^*\phi^*$ appears in each of these surface integrals, and in view of the rapidly decaying property (2), it suffices to require that

$$R^{-1}M_R \to 0 \text{ uniformly, as } R \to \infty, \tag{13}$$

where

$$M_R = \max_{|\boldsymbol{x}^*|=R}\left(|P^*|, |\rho^*\boldsymbol{u}^{*2}|, |\kappa^*\vartheta^*|, |\mu^*\boldsymbol{n}\times\boldsymbol{\omega}^*|\right). \tag{14}$$

The conditions for this to hold can be met, under the assumptions that the boundary layer does not grow indefinitely, the wake behind the finite body does not develop singularities at infinity, nor at finite time, while the shock (whenever it exists) may extend outward indefinitely from the domain concerned.

Let $\boldsymbol{i}$ be the free-stream direction, i.e. $\boldsymbol{c}^* = -c\,\boldsymbol{i}$, then the pressure force along the direction $\boldsymbol{i}$ is obtained by requiring $\nabla^*\phi^*\cdot\boldsymbol{n} = -c\,\boldsymbol{n}\cdot\boldsymbol{i}$ (cf. (6)). The potential function thus required represents exactly the incompressible potential flow induced by the moving body. Collecting the above results and writing them in vector form, we have the pressure force along the direction $\boldsymbol{i}$,

$$\int_{S_0^*}P^*(\boldsymbol{n}\cdot\boldsymbol{i})\,\mathrm{d}A^* = \mathrm{I}^* + \mathrm{II}^* + \mathrm{III}^* + \mathrm{IV}^*, \tag{15a}$$

where

$$\mathrm{I}^* = \frac{1}{c}\int_{V^*} \rho^* \frac{\partial \boldsymbol{u}^*}{\partial t^*} \cdot \nabla^* \phi^* \, \mathrm{d}V^*, \tag{15b}$$

$$\mathrm{II}^* = -\frac{1}{2c}\int_{V^*} \boldsymbol{u}^{*2} \nabla^* \rho^* \cdot \nabla^* \phi^* \, \mathrm{d}V^* - \frac{1}{c}\int_{V^*} \rho^* \boldsymbol{u}^* \times \boldsymbol{\omega}^* \cdot \nabla^* \phi^* \, \mathrm{d}V^*, \tag{15c}$$

$$\mathrm{III}^* = -\frac{1}{c}\int_{S_0^*} \kappa^* \vartheta^* \nabla^* \phi^* \cdot \boldsymbol{n} \, \mathrm{d}A^* + \frac{1}{c}\int_{S_0^*} \mu^* \boldsymbol{n} \times \boldsymbol{\omega}^* \cdot \nabla^* \phi^* \, \mathrm{d}A^*, \tag{15d}$$

$$\mathrm{IV}^* = \frac{1}{c}\int_{V^*} \nabla^* \mu^* \cdot \mathbf{G}^* \cdot \nabla^* \phi^* \, \mathrm{d}V^*, \quad G_{ij}^* = 2\vartheta^* \delta_{ij} + \epsilon_{ijk}\omega_k^* - 2E_{ij}^*. \tag{15e}$$

The right-hand side of (15*a*) has been divided into four parts. Part I* contains the unsteady contribution. Part II* contains two terms, due to the density gradient and vorticity within the flow respectively. Part III* contains two surface integrals, which are called *friction-like terms* to be explained later, while Part IV* is a volume integral due to the gradient of the shear viscosity μ^* within the flow. Each integrand in I*-IV* may be identified as a *source element* of the pressure force; and thus there are six source elements.

At a first glance, the identity (15*a*) does not seem to be appealing since quite a few terms appear in the decomposition. However, not all the source elements are of the same significance at the same time. First of all, in the case of steady flows, we may dispense with the unsteady contributions. Second, it will be demonstrated later that the contribution due to $\nabla^* \mu^*$ is negligible at least in a transonic-to-supersonic regime. For later use, we denote by $R_e^*(\boldsymbol{x}^*)$ and $V_e^*(\boldsymbol{x}^*)$ the two integrands of Part II*:

$$R_e^*(\boldsymbol{x}^*) = -\frac{1}{2c}\boldsymbol{u}^{*2} \nabla^* \rho^* \cdot \nabla^* \phi^*, \quad V_e^*(\boldsymbol{x}^*) = -\frac{1}{c}\rho^* \boldsymbol{u}^* \times \boldsymbol{\omega}^* \cdot \nabla^* \phi^*. \tag{16}$$

Recall from (2) that $\nabla^* \phi^*$ are rapidly decaying. The two elements $R_e^*(\boldsymbol{x}^*)$ and $V_e^*(\boldsymbol{x}^*)$ are negligibly small at distances away from the body. Any finite volume of fluid elements at large distances will therefore not contribute significantly to the aerodynamic forces (lift and drag) through $R_e^*(\boldsymbol{x}^*)$, nor through $V_e^*(\boldsymbol{x}^*)$; this nice property associated with the decomposition (15*a*) is, in our view, satisfactory.

While (15*a*) is the decomposition of the pressure force along the $\boldsymbol{i}$-direction, the friction force projected along the $\boldsymbol{i}$-direction can be shown to be, after a little algebra,

$$-\int_{S_0^*} \tau_{ij}^* n_j \, \mathrm{d}A^* \cdot \boldsymbol{i} = -\int_{S_0^*} \kappa^* \vartheta^* \boldsymbol{n} \cdot \boldsymbol{i} \, \mathrm{d}A^* + \int_{S_0^*} \mu^* \boldsymbol{n} \times \boldsymbol{\omega}^* \cdot \boldsymbol{i} \, \mathrm{d}A^*, \tag{17}$$

where a surface integral of $-2\mu^*(\partial u_j^*/\partial x_i^* - \vartheta^* \delta_{ij})\boldsymbol{n}_j \cdot \boldsymbol{i}$ has been dropped. For (17), we shall denote the first term on the right-hand side by F_1^* and the second term by F_2^*. Likewise, we shall denote by II_1^* the first term of Part II*, and by III_2^* the second term of Part III*. The expressions for the pressure force projected onto other directions can be similarly derived. Let $\boldsymbol{i}$, $\boldsymbol{j}$ and $\boldsymbol{k}$ form an orthonormal set; the components along $\boldsymbol{j}$ and $\boldsymbol{k}$ are obtained by requiring respectively $\nabla^* \phi^* \cdot \boldsymbol{n} = -c\,\boldsymbol{j} \cdot \boldsymbol{n}$ and $\nabla^* \phi^* \cdot \boldsymbol{n} = -c\,\boldsymbol{k} \cdot \boldsymbol{n}$ on the body surface, and then proceeding with the rest in exactly the same way. The unit vector $\boldsymbol{j}$ is typically chosen to be the direction of the lift force. In practice, we need only compute three ϕ^* values, for the directions parallel, normal and transverse to the planform of the delta wing; any other ϕ^* can be obtained by an appropriate linear combination of these three. This is because the unit of any direction can be written as a unique linear combination of a set of three

linearly independent directions. Notice that F_1^* is identical to $-\mathrm{III}_1^*$, and it can be shown that the equality

$$\mathrm{III}_1^* + \mathrm{III}_2^* = -F_1^* + g_e F_2^*, \tag{18}$$

holds for flow about some geometrically simple bodies, e.g. flow about a cylinder, a sphere or an ellipsoid of revolution. The factor g_e is a constant, determined by the shape of the body, and may be termed the geometric factor, which is 1 for a circular cylinder and 0.5 for a sphere. Because of the relation (18), the surface terms of III* in (15*d*) are said to be *friction-like*; and the geometric factor may serve as a measure of the bluffness of geometrically simple bodies (cf. Chang 1992).

4. The method of solution

All the results from now on are presented in dimensionless form. Let the length of reference $\mathscr{L}$ be the distance from the vertex to the base of the delta wing. Time t^* is normalized by $\mathscr{L}/a_\infty^*$, and the density ρ^*, sound speed a^*, temperature T^* are normalized by their values at infinity, ρ_∞^*, a_∞^*, T_∞^*, and so are the viscosities μ^* and λ^* by μ_∞^*. The pressure P^* is normalized by $\rho_\infty^* a_\infty^{*2}$, the velocity $\boldsymbol{u}^*$ by the sound speed a_∞^*, and the auxiliary potential velocity $\nabla^*\phi^*$ is normalized by the speed c. All the normalized variables will be denoted by plain letters. Furthermore, since a turbulence model is to be used, the averaged quantities of the dimensionless physical variables will be denoted with an overbar.

4.1. *Force formula with the turbulence model*

To include the effect of turbulence, we adopt the isotropic algebraic two-layer eddy-viscosity model, originally developed by Baldwin & Lomax (1978) with modifications by Degani & Schiff (1986). Favré's method of averaging (i.e. density-weighted) is taken in the present study. The dimensionless Reynolds-averaged Navier–Stokes equations with the Mach number defined by $M_\infty = u_\infty^*/a_\infty^*$, and the Reynolds number by $Re = \rho_\infty^* u_\infty^* \mathscr{L}/\mu_\infty^*$ then read

$$-\frac{\partial \bar{P}}{\partial x_i} = \bar{\rho}\left(\frac{\partial \bar{u}_i}{\partial t} + \bar{u}_j \frac{\partial \bar{u}_i}{\partial x_j}\right) - \frac{M_\infty}{Re}\frac{\partial \hat{\tau}_{ij}}{\partial x_j}, \tag{19}$$

where $\hat{\tau}_{ij} = -\frac{2}{3}\mu_e \bar{\vartheta}\delta_{ij} + 2\mu_e \bar{E}_{ij}$ with the Stokes' relation $3\lambda_e + 2\mu_e = 0$ being assumed. The pressure $\bar{P}$ is understood to have incorporated a term $\frac{2}{3}\bar{\rho}k$ where k denotes the turbulent kinetic energy. The effective viscosity $\mu_e = \mu_l + \mu_t$ is obtained by evaluating μ_l (molecular viscosity) from Sutherland's law, and μ_t (eddy viscosity) from Baldwin & Lomax's two-layer equilibrium eddy-viscosity model. For details, we refer to Marvin (1983) for the averaged equations, and to Gee, Cummings & Schiff (1992) or Degani & Schiff (1986) for the model of turbulence.

A few words should be added here. It is nowadays common practice to have the turbulence model for $M_\infty < 5$ in the form developed for incompressible flows. The density and temperature fluctuations are considered to have insignificant influence on the model of turbulence. This is called Morkovin's hypothesis; refer to Marvin (1983) and also Lakshminarayana (1986) for a discussion of this aspect. Notice that equation (19) is now in exact analogy with (5) except for the factor M_∞/Re appearing in front of the stress tensor $\hat{\tau}_{ij}$; the appropriate form of (15*a*) for the present model of turbulence is then readily available:

$$\int_{S_0} \bar{P}(\boldsymbol{n}\cdot\boldsymbol{i})\,\mathrm{d}A = \bar{\mathrm{I}} + \overline{\mathrm{II}} + \frac{M_\infty}{Re}\overline{\mathrm{III}} + \frac{M_\infty}{Re}\overline{\mathrm{IV}}, \tag{20a}$$

while the terms on the right-hand side can be written immediately from (15*b–e*):

$$\bar{\mathrm{I}} = \int_V \bar{\rho}\,\frac{\partial \bar{\boldsymbol{u}}}{\partial t}\cdot\nabla\phi\,\mathrm{d}V, \tag{20b}$$

$$\overline{\mathrm{II}} = -\frac{1}{2}\int_V \bar{\boldsymbol{u}}^2\nabla\bar{\rho}\cdot\nabla\phi\,\mathrm{d}V - \int_V \bar{\rho}\bar{\boldsymbol{u}}\times\bar{\boldsymbol{\omega}}\cdot\nabla\phi\,\mathrm{d}V, \tag{20c}$$

$$\overline{\mathrm{III}} = -\int_{S_0}\kappa_e\,\bar{\vartheta}\,\nabla\phi\cdot\boldsymbol{n}\,\mathrm{d}A + \int_{S_0}\mu_e\,\boldsymbol{n}\times\bar{\boldsymbol{\omega}}\cdot\nabla\phi\,\mathrm{d}A, \tag{20d}$$

$$\overline{\mathrm{IV}} = \int_V \nabla\mu_e\cdot\bar{\mathbf{G}}\cdot\nabla\phi\,\mathrm{d}V,\quad \bar{G}_{ij} = 2\bar{\vartheta}\,\delta_{ij} + \epsilon_{ijk}\bar{\omega}_k - 2\bar{E}_{ij}, \tag{20e}$$

where $\kappa_e = \lambda_e + 2\mu_e = (4/3)\mu_e$. In particular, we notice that κ^*, μ^* in (15*d*) and (15*e*) have changed to κ_e, μ_e in (20*d*) and (20*e*) to account for the turbulence effect. The symbols $\bar{\mathrm{I}}$–$\overline{\mathrm{IV}}$ (and also $\bar{F}$) therefore mean that all the other variables in I^*–IV^* (and also F^*) are simply replaced by their averaged and non-dimensionalized quantities. Notice that all the terms (integrands) in (20*b–e*) can be evaluated directly by employing the computed solutions, and in particular, we have now the averaged and non-dimensionalized source elements

$$\bar{R}_e(\boldsymbol{x}) = -\tfrac{1}{2}\bar{\boldsymbol{u}}^2\nabla\bar{\rho}\cdot\nabla\phi \quad\text{and}\quad \bar{V}_e(\boldsymbol{x}) = -\bar{\rho}\bar{\boldsymbol{u}}\times\bar{\boldsymbol{\omega}}\cdot\nabla\phi. \tag{21}$$

4.2. *Numerical method and grid specification*

For numerical purposes, we introduce the general coordinates (ξ,η,ζ):

$$\xi = \xi(x,y,z),\quad \eta = \eta(x,y,z),\quad \zeta = \zeta(x,y,z). \tag{22}$$

The Jacobian J is defined to be $J = \partial(\xi,\eta,\zeta)/\partial(x,y,z)$. The fluid is assumed to be a calorically perfect gas with the specific ratio $\gamma = 1.4$. Let $\bar{\boldsymbol{Q}} = J^{-1}(\bar{\rho},\bar{\rho}\bar{u},\bar{\rho}\bar{v},\bar{\rho}\bar{w},\bar{e})^T$ with $\bar{u}$, $\bar{v}$, $\bar{w}$ the velocity components and $\bar{e}$ the specific total energy (per unit volume). The governing equations, including (19), can be conveniently expressed in the form of conservation laws,

$$\frac{\partial\bar{\boldsymbol{Q}}}{\partial t} + \frac{\partial\bar{\boldsymbol{E}}}{\partial\xi} + \frac{\partial\bar{\boldsymbol{F}}}{\partial\eta} + \frac{\partial\bar{\mathbf{G}}}{\partial\zeta} = \frac{\partial\bar{\boldsymbol{E}}_v}{\partial\xi} + \frac{\partial\bar{\boldsymbol{F}}_v}{\partial\eta} + \frac{\partial\bar{\mathbf{G}}_v}{\partial\zeta} \tag{23}$$

where a subscript 'v' is used to denote viscous or conducting terms, and we refer to Yokota (1990) for the detailed (dimensional) expressions of the flux terms $\bar{\boldsymbol{E}}$, $\bar{\boldsymbol{F}}$, $\bar{\mathbf{G}}$ and $\bar{\boldsymbol{E}}_v$, $\bar{\boldsymbol{F}}_v$, $\bar{\mathbf{G}}_v$ (with the eddy-viscosity turbulence model).

The supplementary conditions for solving (23) are as follows. The flow is assumed to be symmetric about the vertical plane passing through the minor axes of the elliptic cross-sections. The initial condition is that of an impulsive start, while the boundary conditions on the surface of the delta wing are the no-slip, adiabatic and impermeable conditions. In addition, there is a numerical outer boundary where characteristic boundary conditions are imposed for the pressure, density and velocity.

Let $\bar{\boldsymbol{A}} = \partial\bar{\boldsymbol{E}}/\partial\bar{\boldsymbol{Q}}$, $\bar{\boldsymbol{B}} = \partial\bar{\boldsymbol{F}}/\partial\bar{\boldsymbol{Q}}$ and $\bar{\mathbf{C}} = \partial\bar{\mathbf{G}}/\partial\bar{\boldsymbol{Q}}$. The conservation laws (23) are then solved for $\Delta\bar{\boldsymbol{Q}} = \bar{\boldsymbol{Q}}^{n+1} - \bar{\boldsymbol{Q}}^n$ by the following implicit finite-difference scheme between two time levels n and $n+1$:

$$[\boldsymbol{I} + \beta\Delta t(\mathrm{D}_\xi\bar{\boldsymbol{A}} + \mathrm{D}_\eta\bar{\boldsymbol{B}} + \mathrm{D}_\zeta\bar{\mathbf{C}})]\Delta\bar{\boldsymbol{Q}} + \Delta t\,\bar{\mathbf{R}} = \mathbf{0} \tag{24}$$

where Δt is the time step size, and $0 \leqslant \beta \leqslant 1$ specifies the degree of implicitness and

is taken to be 1/2 in the present study. The size of Δt depends on the CFL number and may vary for each time step, and $\bar{\mathbf{R}}$ in (24) denotes the residual term given by

$$\bar{\mathbf{R}} = \mathrm{D}_\xi(\bar{\boldsymbol{E}} + \bar{\boldsymbol{E}}_v) + \mathrm{D}_\eta(\bar{\boldsymbol{F}} + \bar{\boldsymbol{F}}_v) + \mathrm{D}_\zeta(\bar{\mathbf{G}} + \bar{\mathbf{G}}_v), \tag{25}$$

for which $\mathrm{D}_\xi\bar{\boldsymbol{E}}$, $\mathrm{D}_\eta\bar{\boldsymbol{F}}$ and $\mathrm{D}_\zeta\bar{\mathbf{G}}$ will undergo TVD-type discretization (cf. Yee & Harten 1987), while $\mathrm{D}_\xi\bar{\boldsymbol{E}}_v$, $\mathrm{D}_\eta\bar{\boldsymbol{F}}_v$ and $\mathrm{D}_\zeta\bar{\mathbf{G}}_v$ are simply discretized by central finite differencing. Let $\lambda_{\bar{A}}$, $\lambda_{\bar{B}}$ and $\lambda_{\bar{C}}$ denote respectively the eigenvalues of the matrices $\bar{\boldsymbol{A}}$, $\bar{\boldsymbol{B}}$ and $\bar{\boldsymbol{C}}$. To save storage and computational labour, we choose Jameson & Yoon's (1987) LU-SSOR scheme, which makes an approximate factorization of the operator on the left-hand side of (24) to yield

$$\left[\boldsymbol{I} + \beta\Delta t\left(\mathrm{D}_\xi^-\bar{\boldsymbol{A}}^+ + \mathrm{D}_\eta^-\bar{\boldsymbol{B}}^+ + \mathrm{D}_\zeta^-\bar{\boldsymbol{C}}^+ - \bar{\boldsymbol{A}}^- - \bar{\boldsymbol{B}}^- - \bar{\boldsymbol{C}}^-\right)\right]$$

$$\times\left[\boldsymbol{I} + \beta\Delta t\left(\mathrm{D}_\xi^+\bar{\boldsymbol{A}}^- + \mathrm{D}_\eta^+\bar{\boldsymbol{B}}^- + \mathrm{D}_\zeta^+\bar{\boldsymbol{C}}^- + \bar{\boldsymbol{A}}^+ + \bar{\boldsymbol{B}}^+ + \bar{\boldsymbol{C}}^+\right)\right]\Delta\bar{\boldsymbol{Q}} = -\Delta t\,\boldsymbol{M}\bar{\mathbf{R}}, \tag{26}$$

where

$$\boldsymbol{M} = [1 + \beta\Delta t\,(v_{\bar{A}} + v_{\bar{B}} + v_{\bar{C}})]\,\boldsymbol{I}. \tag{27}$$

The symbols D_ξ^+, D_η^+, D_ζ^+ denote forward-difference operators in the respective directions, while D_ξ^-, D_η^-, D_ζ^- are backward-difference operators, and

$$\bar{\boldsymbol{A}}^+ = \frac{1}{2}(\bar{\boldsymbol{A}} + v_{\bar{A}}\boldsymbol{I}), \quad \bar{\boldsymbol{A}}^- = \frac{1}{2}(\bar{\boldsymbol{A}} - v_{\bar{A}}\boldsymbol{I}), \tag{28a}$$

$$\bar{\boldsymbol{B}}^+ = \frac{1}{2}(\bar{\boldsymbol{B}} + v_{\bar{B}}\boldsymbol{I}), \quad \bar{\boldsymbol{B}}^- = \frac{1}{2}(\bar{\boldsymbol{B}} - v_{\bar{B}}\boldsymbol{I}), \tag{28b}$$

$$\bar{\boldsymbol{C}}^+ = \frac{1}{2}(\bar{\boldsymbol{C}} + v_{\bar{C}}\boldsymbol{I}), \quad \bar{\boldsymbol{C}}^- = \frac{1}{2}(\bar{\boldsymbol{C}} - v_{\bar{C}}\boldsymbol{I}), \tag{28c}$$

with

$$v_{\bar{A}} \geqslant \max(|\lambda_{\bar{A}}|), \quad v_{\bar{B}} \geqslant \max(|\lambda_{\bar{B}}|), \quad v_{\bar{C}} \geqslant \max(|\lambda_{\bar{C}}|). \tag{29}$$

To complete the numerical procedure, it remains to specify the grid system, for which ξ, η and ζ take on integral values on the grid points. Between $x = 0$ and 1, ξ is related to x by

$$x = 1 - \delta_1\frac{K_1 - 1}{K_1 + 1} \quad \text{with} \quad K_1(\xi) = \left(\frac{\delta_1 + 1}{\delta_1 - 1}\right)^{1-(\xi/p)}, \tag{30}$$

where p is the largest value of ξ, and $\delta_1 > 1$ is a parameter, which implies a dense grid distribution near the solid boundary as δ_1 is close to 1. In addition, a number of grid points are also put along the negative x-direction between $x = -c$ and 0 and $x = 1$ and d in a way similar to (30). Let A, B be two constants; we write for each ξ,

$$y = a(\xi,\eta)\cos\theta(\zeta), \quad z = b(\xi,\eta)\sin\theta(\zeta), \tag{31}$$

$$\frac{a(\xi,\eta) - a(\xi)}{A - a(\xi)} = 1 - \delta_2\frac{K_2 - 1}{K_2 + 1} = \frac{b(\xi,\eta) - b(\xi)}{B - b(\xi)}, \tag{32}$$

where $2a(\xi)$ and $2b(\xi)$ denote the lengths of the major and minor axes of the elliptic section. $K_2(\eta)$ is made identical to $K_1(\xi)$ by merely replacing (p, ξ, δ_1) by (q, η, δ_2). The variable ζ is scaled with the azimuthal angle θ: $\zeta = r\theta/\pi$ which is equally divided: $\Delta\theta = \pi/r$ ($\Delta\zeta = 1$). The numerical outer boundary is determined by the two planes $x = -c$ (ahead of the vertex) and $x = d$, and the surface of an elliptic cylinder described by $(x/A)^2 + (y/B)^2 = 1$.

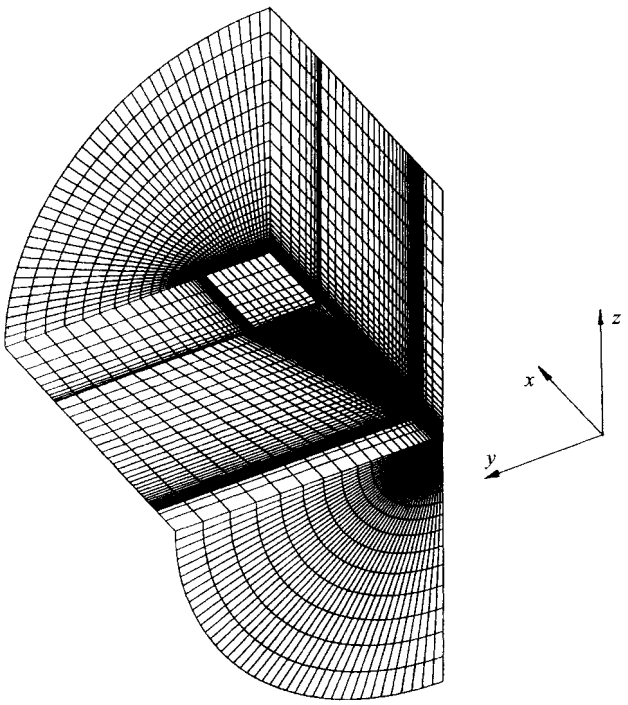

FIGURE 2. The grid system adopted in the present study; between $x = 1$ and $d = 1.5$, the grid is shown for the planar section $z = 0$.

The overall scheme constructed is second order in both time and space, and allows a CFL number of 5. Figure 2 shows the grid system adopted here, which is one with $p \times q \times r = 30 \times 40 \times 80$ and has, in addition, five points ahead of the vertex along the negative x–direction. Behind the trailing-edge plane, the grid system is $15 \times 50 \times 80$ where 10 η-grid lines are appended to account for the part of the wake directly behind the base of the delta wing. It is found adequate to take $c = 0.2$, $d = 1.5$ and $\delta_1 = 1.03$ for the scaling between x and ξ, and $A = B = 1.5$, $\delta_2 = 1.0005$ for the scaling between η and $a(\xi, \eta)$ and $b(\xi, \eta)$. This choice gives the smallest spacings: $\Delta x_0 = 4.45 \times 10^{-3}$, and $a(\xi, 1) - a(\xi) = 1.152 \times 10^{-4}(1.5 - a(\xi))$. Let N be the total number of grid points; steady-state solutions are obtained by requiring the L_2 norm $N^{-1/2}[\sum(\rho^{n+1} - \rho^n)^2]^{1/2}$ of two successive density distributions ρ^n and ρ^{n+1} on the grid to be less than 4×10^{-6}. The same grid system is also used to solve for the auxiliary potential functions ϕ, defined in the previous sections. All the calculations are performed on a CRAY-YMP/EL, and the CPU time for the numerical scheme is on the average 2×10^{-4} s per grid point per time step.

5. Numerical results and discussion

The Reynolds number Re is taken to be 10^6 for all the cases, at which and for the present geometry, the assumption (13) with (14) can be considered to be valid.

Since no existing turbulence model is known to be satisfactory for all separated flows, it is necessary to assess the validity of the adopted model by comparison with experimental data. Figure 3 shows the computed surface pressure coefficients C_P at two different sections, compared to the experimental values measured by Squire

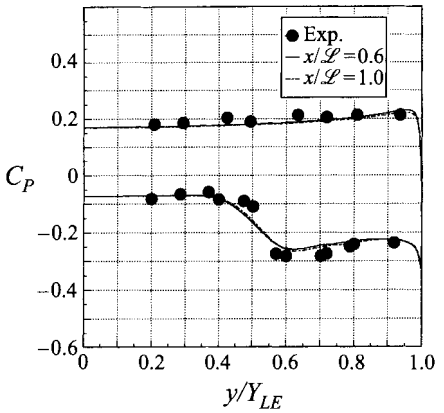

FIGURE 3. Computed surface pressure coefficient C_P, compared to the values measured by Squire (1985) for the case $M_\infty = 1.8$, $\alpha = 10°$ and $Re = 10^6$, where Y_{LE} denotes one-half length of the major axis.

(1985). The agreement appears to be satisfactory, and a good conical symmetry is revealed in this case. Let S^* be a reference area with $S = 1/4$. The lift coefficient is defined by

$$C_L = \frac{\bar{L}^*}{\frac{1}{2}\rho_\infty^* u_\infty^{*2} S^*} = \frac{\bar{L}}{\frac{1}{2}M_\infty^2 S}, \tag{33}$$

where $\bar{L}^*$ ($\bar{L}$) denotes the averaged (dimensionless) lift exerted on the delta wing. The drag coefficient C_D is defined in the same way. It should be noted here that C_D and C_L are evaluated according to the averaged version of (4), i.e.,

$$\int_{S_0} \bar{P}\, n_i \,\mathrm{d}A - \frac{M_\infty}{Re} \int_{S_0} \hat{\tau}_{ij} n_j \,\mathrm{d}A, \tag{34}$$

where the stress tensor $\hat{\tau}_{ij}$ is defined below (19), and may be computed by analogy with (17). Figure 4 presents the general behaviour of the lift and drag coefficients. It is observed that for each M_∞, both C_L and C_D increase monotonically with increasing angle of attack α. The maximum lift to drag ratio is 3, occurring at around $\alpha = 10°$ for all the Mach numbers M_∞ considered. For each α, both C_L and C_D decrease monotonically with increasing Mach number M_∞. Inspecting the individual lift and drag curves for various M_∞ reveals that the rate of increase with α for both C_L and C_D is getting slower at higher Mach numbers. The lift curve for $M_\infty = 1.8$ even bends downward, and which means that we can no longer increase the lift coefficient efficiently by increasing further the angle of attack α at this higher Mach number.

5.1. *Basic flow patterns*

It would be useful to first identify the flow pattern. Newsome (1986) investigated the same profile; his study was however limited to the Mach number $M_\infty = 2.0$ and the angle of attack $\alpha = 10°$. It is therefore worthwhile to have a discussion about the flow structures. Figure 5(*a*) shows the basic flow pattern, while 5(*b*) shows a typical section. Since the flow is symmetric about the vertical plane crossing the centreline, our discussion will be limited to the left half-plane for convenience. (Notice that conical symmetry is not assumed in the present study.) Typically, the flow separates along a line near the leading edge, leading to a primary vortex (PV). The line of separation is called the primary separation line (PSL). In most cases, the primary vortex is strong

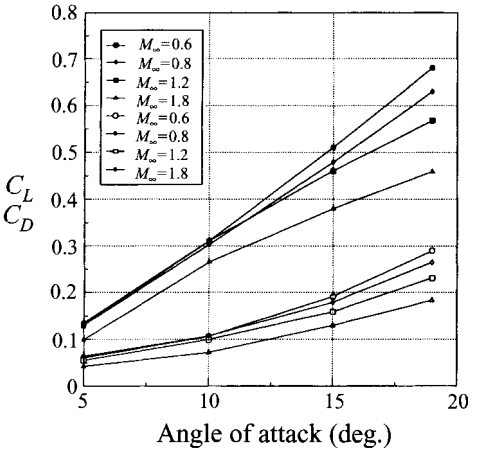

FIGURE 4. Lift (C_L: upper curves) and drag (C_D: lower curves) coefficients at various Mach numbers M_∞ and angles of attack α.

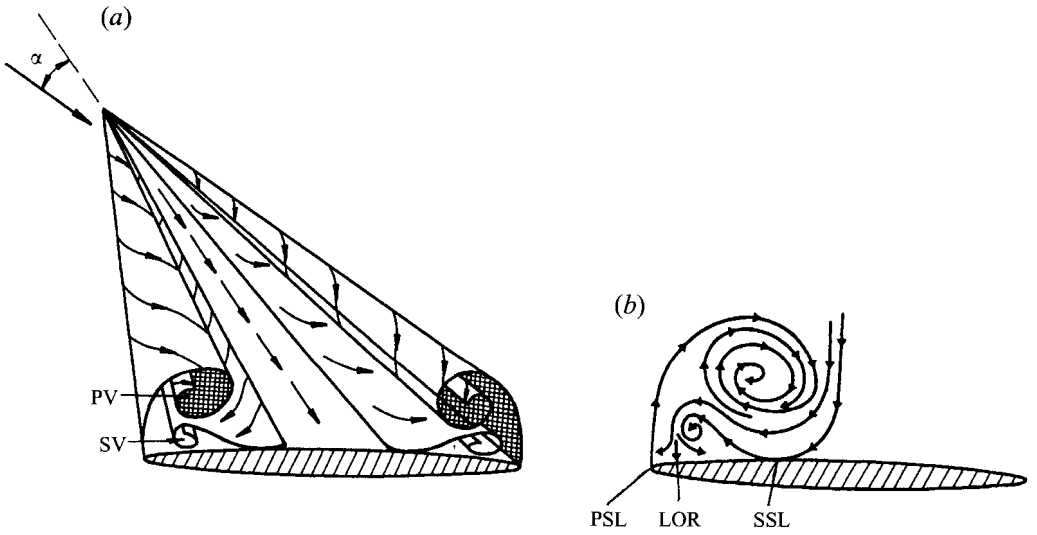

FIGURE 5. Typical flow pattern: (*a*) an overview, (*b*) a cross-section.

enough to cause a secondary separation along another line, leading to a secondary vortex (SV) or separation bubble. This line of separation will be termed the secondary separation line (SSL). The primary vortex reattaches to the surface of the delta wing along a third line of interest – termed the line of reattachment (LOR). The relative positions of these highlighted lines reveal much flow information. Another region of importance is the front boundary layer lying in front of (below) the delta wing, and a shock may exist below the delta wing at relatively high Mach numbers.

5.2. *Limiting surface streamlines*

In order to see how the lines mentioned above and other detailed features behave under different M_∞ and α, it is probably informative to investigate the limiting surface streamlines on the delta wing.

Figure 6 shows limiting surface streamlines for $M_\infty = 0.6$ at $\alpha = 5°$, 10° and 19°. The primary separation line is near the edge at $\alpha = 5°$, moving rapidly toward the

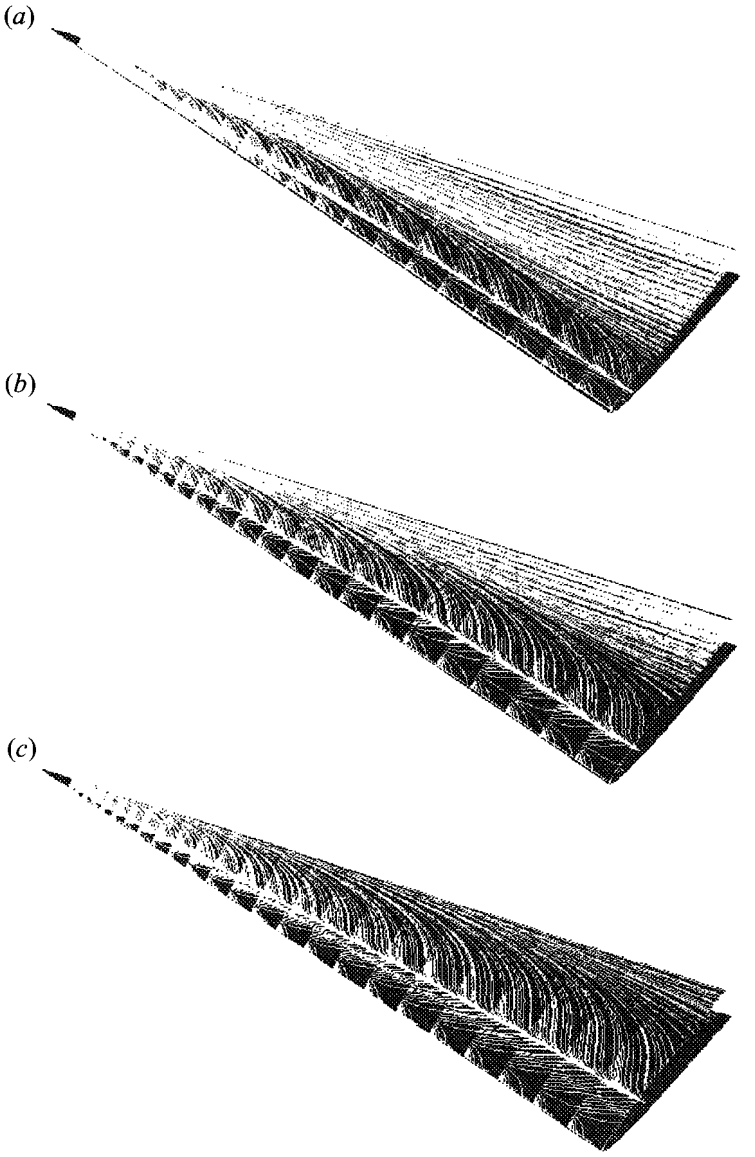

FIGURE 6. Limiting surface streamlines for $M_\infty = 0.6$: (*a*) $\alpha = 5°$, (*b*) 10° and (*c*) 19°.

leading edge with increasing α. Meanwhile, the secondary separation line and the line of reattachment move in the inboard direction and their distance is widening. The last fact indicates that the secondary vortex grows in size and moves inboard with increasing α. It is also seen that the whole region of cross-flow is extending inboard with increasing α. This implies that the primary vortex covers a wider flow region at higher α, say 19°, extending from the leading edge to an inner line close to plane of symmetry. For $M_\infty = 0.8$ and 1.2, we have very similar patterns of limiting surface streamlines, but the secondary vortex is smaller at $\alpha = 5°$ and is somewhat larger at higher $\alpha = 10°$ and 19°. Figure 7 shows the plots of limiting surface streamlines for $M_\infty = 1.8$ at $\alpha = 5°$, 10° and 19°. The secondary vortex barely exists at $\alpha = 5°$, and is typically smaller than it is at lower Mach number at the same angle of attack. If we look at the density profiles (not shown), the flow structures over the delta wing

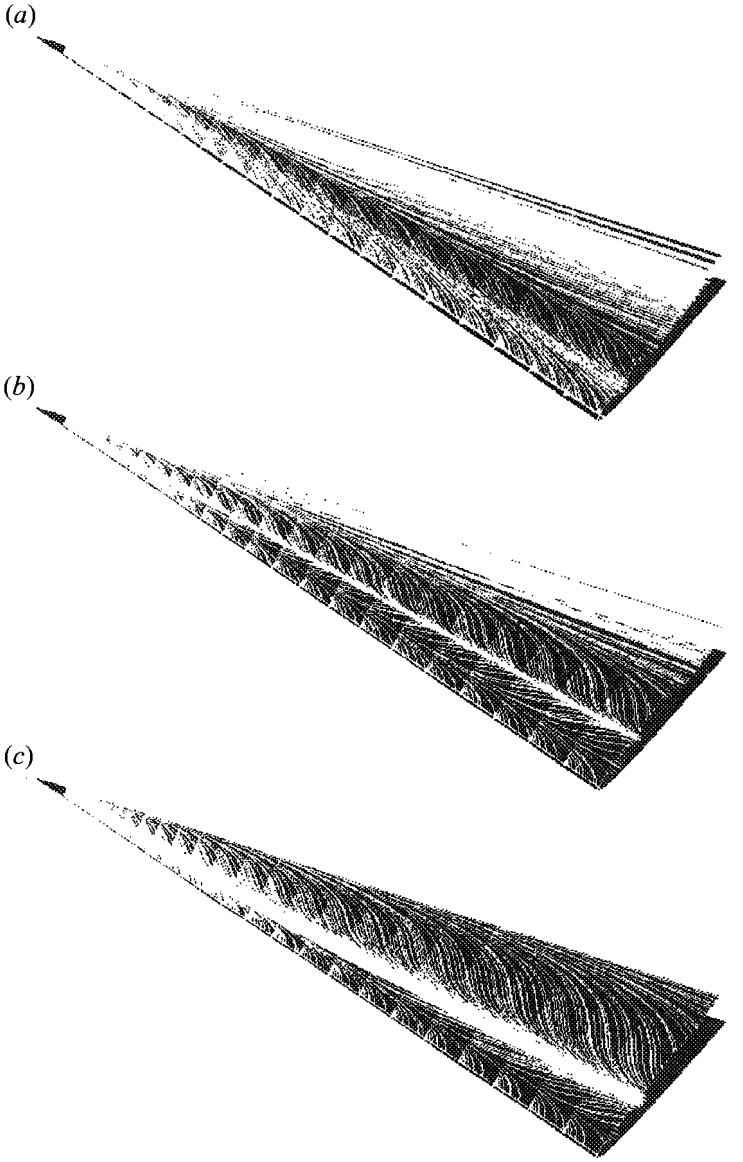

FIGURE 7. Limiting surface streamlines for $M_\infty = 1.8$: (*a*) $\alpha = 5°$, (*b*) 10° and (*c*) 19°.

appear to be more flat at higher Mach numbers, and near the leading edge there is a region of strong expansion as the flow turns around it.

5.3. *Analysis of the lift force*

It is found by evaluating the individual contributions for all the cases under consideration that about 95% or even more of the lift coefficient C_L comes from C_{LR} and C_{LV}. Here C_{LR} and C_{LV} are defined as follows:

$$C_{LR}(C_{LV}) : \text{the part of } C_L \text{ due to } \bar{R}_e(\boldsymbol{x})(\bar{V}_e(\boldsymbol{x}))$$

in front of the plane passing through the trailing edge. (Note that in the present section $\bar{R}_e(\boldsymbol{x})$ and $\bar{V}_e(\boldsymbol{x})$ are used exclusively to denote the lift (not drag) elements.) To illustrate this situation, table 1 lists the individual contributions of the various source

	Source	$\alpha = 5°$	$\alpha = 10°$	$\alpha = 15°$	$\alpha = 19°$
(*a*)	$\overline{\mathrm{I}}'$	–	–	–	–
	$\overline{\mathrm{II}}_1'(C_{LR})$	0.038407	0.093312	0.152990	0.217646
	$\overline{\mathrm{II}}_2'(C_{LV})$	0.092982	0.208384	0.341448	0.451945
	$\overline{\mathrm{III}}_1'$	0.000874	0.002232	0.003561	0.004085
	$\overline{\mathrm{III}}_2'$	0.000782	0.001464	0.001836	0.002095
	$\overline{\mathrm{IV}}'$	−0.000002	0.000003	0.000013	0.000023
	$\overline{F}_1'$	0.000874	0.002232	0.003561	0.004085
	$\overline{F}_2'$	0.000356	0.000826	0.001286	0.001706
	R_m	−0.000182	0.002039	0.004141	0.001518
	C_L(Total)	0.134091	0.310492	0.508836	0.683103
(*b*)	$\overline{\mathrm{I}}'$	–	–	–	–
	$\overline{\mathrm{II}}_1'(C_{LR})$	0.062136	0.149082	0.243051	0.320445
	$\overline{\mathrm{II}}_2'(C_{LV})$	0.063921	0.142731	0.223529	0.300688
	$\overline{\mathrm{III}}_1'$	0.000864	0.002189	0.003116	0.004021
	$\overline{\mathrm{III}}_2'$	0.000778	0.001497	0.002009	0.002192
	$\overline{\mathrm{IV}}'$	−0.000011	0.000002	0.000015	0.000270
	$\overline{F}_1'$	0.000864	0.002189	0.003116	0.004021
	$\overline{F}_2'$	0.000386	0.000805	0.001202	0.001559
	R_m	0.000773	0.004152	0.003373	0.001895
	C_L(Total)	0.129711	0.302647	0.479411	0.635091
(*c*)	$\overline{\mathrm{I}}'$	–	–	–	–
	$\overline{\mathrm{II}}_1'(C_{LR})$	0.127123	0.304337	0.459511	0.553925
	$\overline{\mathrm{II}}_2'(C_{LV})$	−0.002807	−0.993842	−0.005170	−0.002098
	$\overline{\mathrm{III}}_1'$	0.000742	0.002107	0.003023	0.003939
	$\overline{\mathrm{III}}_2'$	0.000738	0.001223	0.001762	0.002002
	$\overline{\mathrm{IV}}'$	−0.000028	0.000003	0.000017	0.000034
	$\overline{F}_1'$	0.000742	0.002107	0.003023	0.003939
	$\overline{F}_2'$	0.000374	0.000801	0.001170	0.001490
	R_m	0.003265	0.003592	-0.000335	0.005181
	C_L(Total)	0.130149	0.310328	0.463001	0.568412
(*d*)	$\overline{\mathrm{I}}'$	–	–	–	–
	$\overline{\mathrm{II}}_1'(C_{LR})$	0.203109	0.484125	0.696120	0.813921
	$\overline{\mathrm{II}}_2'(C_{LV})$	−0.107029	−0.231251	−0.324431	−0.368490
	$\overline{\mathrm{III}}_1'$	0.000597	0.001007	0.001416	0.001906
	$\overline{\mathrm{III}}_2'$	0.000394	0.000782	0.001120	0.001612
	$\overline{\mathrm{IV}}'$	−0.000058	0.000441	−0.000026	0.005996
	$\overline{F}_1'$	0.000597	0.001007	0.001416	0.001906
	$\overline{F}_2'$	0.000356	0.000772	0.001080	0.001563
	R_m	0.000346	0.007429	0.007256	0.000597
	C_L(Total)	0.098312	0.264312	0.383950	0.459011

TABLE 1. Relative importance of source elements where $\overline{\mathrm{I}}_1', \ldots, \overline{F}_2'$ denote respectively $\overline{\mathrm{I}}_1', \ldots, \overline{F}_2'$ restricted to the flow field in front of the trailing-edge plane. Note that $\overline{F}_1'$ and $\overline{\mathrm{III}}_1'$ are displayed for their absolute values, while R_m is defined to be the difference between the total lift coefficient C_L and the sum of the above contributions. (*a*) $M_\infty = 0.6$, (*b*) $M_\infty = 0.8$, (*c*) $M_\infty = 1.2$, (*d*) $M_\infty = 1.8$.

elements for all the cases under consideration. Notice that there is a difference R_m between the computed C_L and the sum of all the force integrals because the domain of computation is limited. However, the smalless of R_m, compared to the value of C_L, observed in all the cases not only gives us some confidence in the numerical results, but also provides a good indication that the present analysis based on the expression (20*a*) is useful and meaningful.

The friction and friction-like terms: $\overline{F}$, $\overline{\mathrm{III}}$ as well as $\overline{\mathrm{IV}}$ are also found to be relatively insignificant. C_{LR} and C_{LV} are therefore of primary interest for further investigation. Meanwhile, it would be also of interest to look into the distributions of $\bar{R}_e(\boldsymbol{x})$ and $\bar{V}_e(\boldsymbol{x})$ (cf. (21)) in some selected cases. In view of (33), we define

$$\hat{R}_e(\boldsymbol{x}) = \frac{\bar{R}_e(\boldsymbol{x})}{\frac{1}{2}M_\infty^2 S} \quad \text{and} \quad \hat{V}_e(\boldsymbol{x}) = \frac{\bar{V}_e(\boldsymbol{x})}{\frac{1}{2}M_\infty^2 S}. \tag{35}$$

To understand further the behaviour of C_{LR} and C_{LV}, we divide the computed flow region into the windward and the leeward sides, and observe the total contributions of $\hat{R}_e(\boldsymbol{x})$ and $\hat{V}_e(\boldsymbol{x})$ in individual regions. $C_{LV}(w)$, $C_{LR}(l)$ and $C_{LV}(w)$, $C_{LV}(l)$ are used to denote these individual contributions; though the partition is somewhat arbitrary, it does reflect salient features of the source elements $\hat{R}_e(\boldsymbol{x})$ and $\hat{V}_e(\boldsymbol{x})$.

5.3.1. $M_\infty = 0.6$, $\alpha = 5°$, $10°$, $15°$, $19°$

Figure 8(*a*) shows that C_{LR} increases more rapidly than C_{LV} with increasing angle of attack. Observe that C_{LV} contributed by $V_e(\boldsymbol{x})$ is twice as much as C_{LR} contributed by $\hat{R}_e(\boldsymbol{x})$ for all the the angles of attack. For this subsonic case, $\hat{V}_e(\boldsymbol{x})$ rather than $\hat{R}_e(\boldsymbol{x})$ is the dominating contributor to the lift. Next let us look at the individual contributions from the leeward and windward sides. Figure 8(*b*) shows the decomposition $C_{LR} = C_{LR}(l)+C_{LR}(w)$, while figure 8(*c*) shows $C_{LV} = C_{LV}(l)+C_{LV}(w)$. It is seen that $C_{LR}(w)$ is fairly small and increases slowly to 0.065 at $\alpha = 19°$, while $C_{LR}(l)$ is relatively important and increases moderately to 0.16 at $\alpha = 19°$. Notice that $C_{LV}(w)$ is *negative*, and its value for each respective angle α is obviously not negligible. The value of C_{LV} is the result due to strong cancellation of $C_{LV}(l)$ from the leeward side by the negative $C_{LV}(w)$ from the windward side. Whilst $C_{LV}(l)$ increases from 0.79 at $\alpha = 5°$ to 0.99 at $\alpha = 19°$, $C_{LV}(w)$ varies gradually from -0.71 at $\alpha = 5°$ to th value -0.53 at $\alpha = 19°$. Although C_{LR} is not very small compared to C_{LV}, the individual components $C_{LR}(l)$ and $C_{LR}(w)$ are smaller than $C_{LV}(l)$ and $C_{LV}(w)$ by one order of magnitude.

5.3.2. $M_\infty = 0.8$, $\alpha = 5°$, $10°$, $15°$, $19°$

Figure 9(*a*) shows that C_{LV} and C_{LR} are of the same order in this high subsonic case. Compared to C_{LV}, the value of C_{LR} increases at a slightly faster pace from 0.067 at $\alpha = 5°$ to 0.33 at $\alpha = 19°$. It is inferred from the present and the previous cases that the element $\hat{R}_e(\boldsymbol{x})$ replaces $\hat{V}_e(\boldsymbol{x})$ as a dominating contributor to the lift at about $M_\infty = 0.75$. Let us also examine the individual contributions from the leeward and windward sides. Figure 9(*b*) shows the decomposition $C_{LR} = C_{LR}(l) + C_{LR}(w)$, while figure 9(*c*) shows $C_{LV} = C_{LV}(l) + C_{LV}(w)$. It is seen that $C_{LR}(w)$ is fairly small and even negative at $\alpha = 5°$, but then increases to the positive value 0.08 at $\alpha = 19°$. $C_{LR}(l)$ is relatively more important, increasing steadily from 0.077 at $\alpha = 5°$ to 0.24 at 19°. Owing to the vorticity, C_{LV} is again due to strong cancellation of $C_{LV}(l)$ from the leeward side by the negative $C_{LV}(w)$ from the windward side. Compared to the previous case, here $C_{LV}(l)$ increases less rapidly with increasing α, being 0.77 at $\alpha = 5°$ and 0.86 at $\alpha = 19°$, while the magnitude of $C_{LV}(w)$ varies at about the

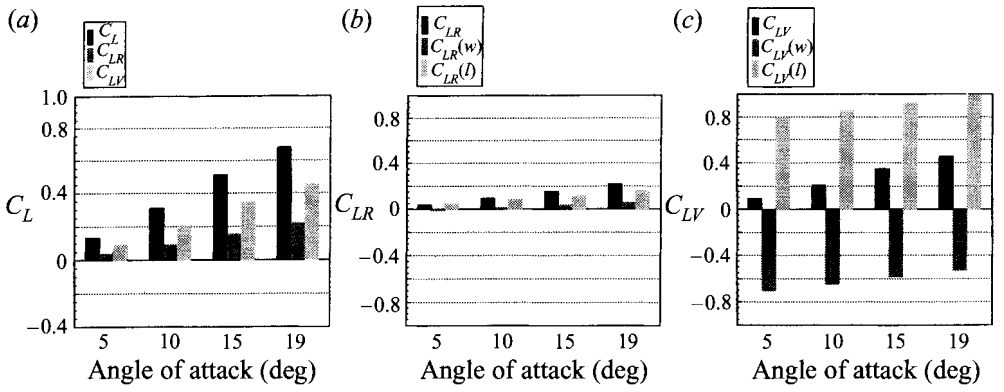

FIGURE 8. Analysis of C_L at $M_\infty = 0.6$: (*a*) contributions to C_L from C_{LR} and C_{LV}, (*b*) decomposition of C_{LR} $(= C_{LR}(w) + C_{LR}(l))$, (*c*) decomposition of C_{LV} $(= C_{LV}(w) + C_{LV}(l))$,

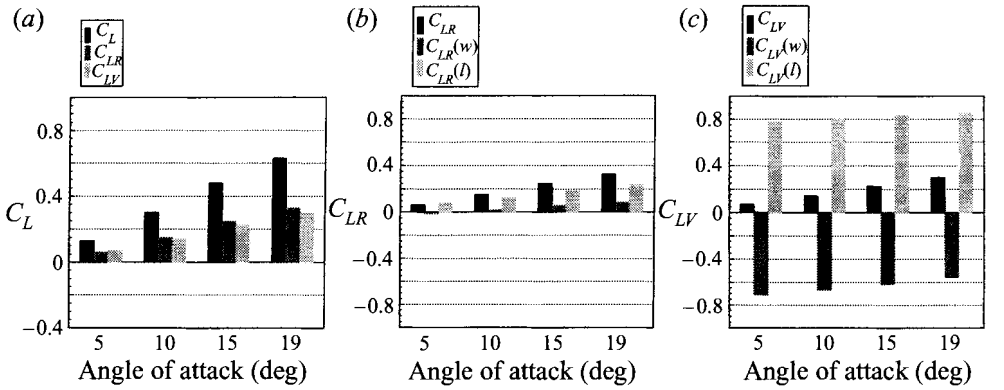

FIGURE 9. As figure 8 but at $M_\infty = 0.8$.

same rate. These trends result in smaller values of C_{LV} at this higher M_∞ at the same angle of attack. The comparison indicates that with increasing M_∞, the vortex systems around the delta wing reinforce the elements $\hat{R}_e(\boldsymbol{x})$, whilst weakening their contribution through $\hat{V}_e(\boldsymbol{x})$. Although C_{LR} and C_{LV} are of comparable order, we observe again that $C_{LR}(l)$ and $C_{LR}(w)$ are much smaller than $C_{LV}(l)$ and $C_{LV}(w)$ in magnitude.

5.3.3. *On the negative sign of* $\hat{V}_e(\boldsymbol{x})$ *and* $C_{LV}(w)$

It would be interesting to understand why the value of $C_{LV}(w)$ is negative – a somewhat surprising result. Obviously, $C_{LV}(w)$ is due to non-vanishing vorticity, and the front boundary layer (below the delta wing) is the only source of vorticity and thus $\hat{V}_e(\boldsymbol{x})$. It is therefore necessary to consider the orientation of $\bar{\boldsymbol{u}} \times \bar{\boldsymbol{\omega}}$ and its inner product with $-\nabla\phi$ of the hypothetical potential ϕ. For this, it is convenient to decompose the free-stream velocity into a component parallel to the wing's planform and the one perpendicular to it (cf. figure 1). Near the front of the wing, M_∞^p induces a transverse vorticity component $\bar{\omega}_t$, while M_∞^v induces a vorticity component $\bar{\omega}_p$ parallel to the direction of M_∞^p. The two components constitute the front boundary layer within which we shall write $\bar{\boldsymbol{u}} = \bar{\boldsymbol{u}}_p + \bar{\boldsymbol{u}}_t$ and $\bar{\boldsymbol{\omega}} = \bar{\boldsymbol{\omega}}_t + \bar{\boldsymbol{\omega}}_p$, thus

$$\bar{\boldsymbol{u}} \times \bar{\boldsymbol{\omega}} = \bar{\boldsymbol{u}}_p \times \bar{\boldsymbol{\omega}}_t + \bar{\boldsymbol{u}}_t \times \bar{\boldsymbol{\omega}}_p.$$

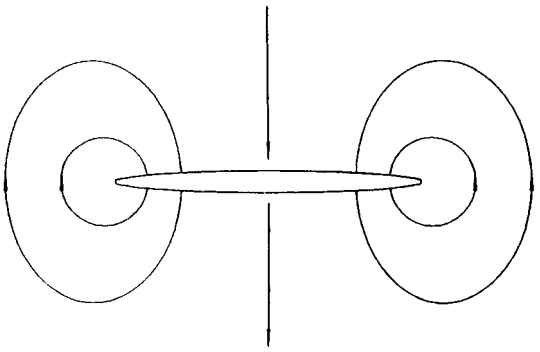

FIGURE 10. Schematic of the hypothetical vector field $\nabla\phi$ associated with the lift with the delta wing moving downward (opposite to the lift direction).

Both terms on the right-hand side are normal to the wing's planform and directed toward the windward side. Since here we consider the lift, $\nabla\phi$ is the velocity of the potential flow, generated by hypothetically moving the delta wing in the direction of negative lift. The orientation of $\nabla\phi$ in a cross-section away from the vertex and the base of the delta wing can be seen from figure 10. Within the front boundary layer, the angle between $\bar{\boldsymbol{u}} \times \bar{\boldsymbol{\omega}}$ and the direction of $\nabla\phi$ is accurately approximated by the angle of attack α. Since the angle of attack α is acute, $\bar{\boldsymbol{u}} \times \bar{\boldsymbol{\omega}} \cdot \nabla\phi$ must necessarily be positive, and thus the element $\bar{V}_e(\boldsymbol{x}) = -\bar{\rho}\bar{\boldsymbol{u}} \times \bar{\boldsymbol{\omega}} \cdot \nabla\phi$ is *negative*. Notice that the range of α is between 5° and 19°, hence the dominating vorticity component is due to M_∞^p (related to $\cos\alpha$) rather than M_∞^v (related to $\sin\alpha$). For a given Mach number M_∞ (0.6 or 0.8), this explains why the negative value of $C_{LV}(w)$ decreases in magnitude with increasing angle of attack α. No effect from the shock is observed to have significance at these relatively low Mach numbers.

5.3.4. $M_\infty = 1.2$, $\alpha = 5°, 10°, 15°, 19°$

Figure 11(*a*) shows C_L decomposed into C_{LR} and C_{LV}. Surprisingly, the lift is contributed almost totally by $\hat{R}_e(\boldsymbol{x})$; the value of C_{LV} contributed by $\hat{V}_e(\boldsymbol{x})$ is negligibly small. Now C_{LV} and C_{LR} are no longer of comparable order of significance in this supersonic case. But then what happens to the vorticity element $\hat{V}_e(\boldsymbol{x})$? To investigate this, we need to examine the individual contributions of $\hat{R}_e(\boldsymbol{x})$ and $\hat{V}_e(\boldsymbol{x})$ from the leeward and windward sides. Figure 11(*b*) shows the decomposition $C_{LR} = C_{LR}(l) + C_{LR}(w)$, while figure 11(*c*) shows $C_{LV} = C_{LV}(l) + C_{LV}(w)$. $C_{LR}(w)$ is negative (−0.04) at $\alpha = 5°$ and increases gradually to 0.12 at 19°. In contrast, $C_{LR}(l)$ is still much more important and increases steadily from 0.16 at $\alpha = 5°$ to 0.43 at $\alpha = 19°$. Addition of $C_{LR}(l)$ and $C_{LR}(w)$ is basically constructive, yielding a positive contribution to the total lift coefficient. In view of all the cases discussed so far, the values of $C_{LR}(l)$ and also $C_{LR}(w)$ increase with increasing Mach number M_∞ at the same angle of attack. Next consider $C_{LV} = C_{LV}(l) + C_{LV}(w)$. The addition is now totally destructive; the positive $C_{LV}(l)$ is well balanced by the negative $C_{LV}(w)$. Notice that here $C_{LV}(l)$ decreases gradually with increasing α, which is in strong contrast to the previous cases of lower Mach numbers, where $C_{LV}(l)$ increases with increasing α. On the other hand, the magnitude of $C_{LV}(w)$ as usual decreases with increasing angle of attack α. $C_{LV}(l)$ decreases from 0.70 at $\alpha = 5°$ to 0.61 at 19°, while $C_{LV}(w)$ increases from −0.70 at $\alpha = 5°$ to −0.61 at 19°. These trends result in nearly total cancellation of $C_{LV}(l)$ by $C_{LV}(w)$, yielding the very small values of C_{LV}. Again, we have observed that by increasing M_∞, the vortex systems over the

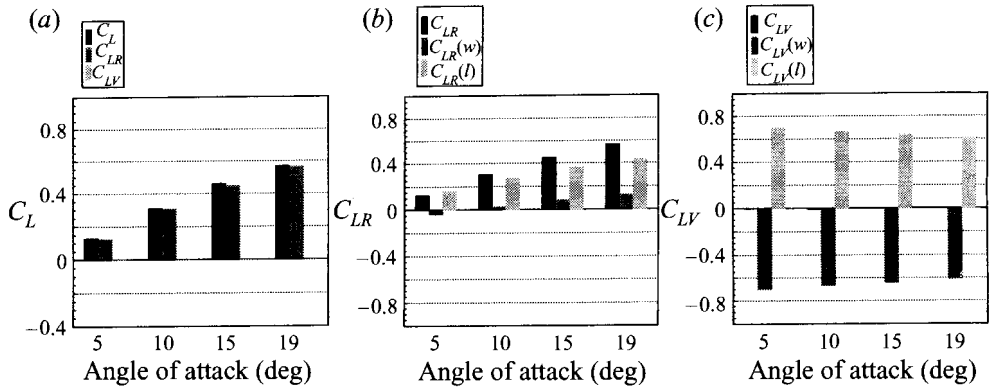

FIGURE 11. Analysis of C_L at $M_\infty = 1.2$: (*a*) contributions to C_L from C_{LR} and C_{LV}, (*b*) decomposition of C_{LR} $(= C_{LR}(w) + C_{LR}(l))$, (*c*) decomposition of C_{LV} $(= C_{LV}(w) + C_{LV}(l))$,

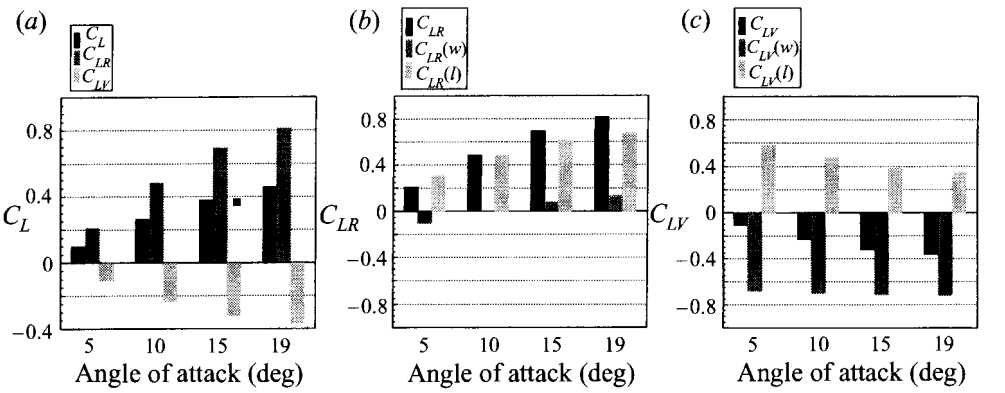

FIGURE 12. As figure 11 but at $M_\infty = 1.8$.

delta wing intensify their contribution to the lift through $\hat{R}_e(\boldsymbol{x})$, whilst weakening the contribution through $\hat{V}_e(\boldsymbol{x})$. Although C_{LR} is negligibly small compared to C_{LV}, note that $C_{LV}(l)$ and $C_{LV}(w)$ are at least of comparable order to $C_{LR}(l)$ and $C_{LR}(w)$.

5.3.5. $M_\infty = 1.8$, $\alpha = 5°, 10°, 15°, 19°$

Figure 12(*a*) shows C_L decomposed into C_{LR} and C_{LV}. At this Mach number, we even see that the value of C_{LV} is negative for all the α values considered. C_{LR} is about 0.2 at $\alpha = 5°$, and increases rapidly to 0.81 at $\alpha = 19°$. On the other hand, C_{LV} is -0.1 at $\alpha = 5°$ and decreases rapidly to -0.36 at $\alpha = 19°$. Although the value of C_{LR}, compared to that at $M_\infty = 1.2$, is relatively much larger for each respective α, the overall lift coefficient C_L is smaller because of the cancellation due to the negative sign of C_{LV}. Figure 12(*b*) shows the decomposition $C_{LR} = C_{LR}(l) + C_{LR}(w)$, while figure 12(c) shows $C_{LV} = C_{LV}(l) + C_{LV}(w)$. $C_{LR}(w)$ is -0.1 at $\alpha = 5°$, but increases gradually to about 0.13 at $\alpha = 19°$. In contrast, $C_{LR}(l)$ is much more important and increases steadily from 0.31 at $\alpha = 5°$ to 0.67 at $\alpha = 19°$. Addition of $C_{LR}(l)$ and $C_{LR}(w)$ is constructive except at $\alpha = 5°$, yielding a positive contribution of C_{LR} to the lift. On the other hand, the addition $C_{LV} = C_{LV}(l) + C_{LV}(w)$ is destructive; the positive $C_{LV}(l)$ is cancelled to a large extent by the negative $C_{LV}(w)$. $C_{LV}(l)$ decreases from 0.57 at $\alpha = 5°$ to 0.35 at $\alpha = 19°$. Notice that the negative $C_{LV}(w)$ even decreases slowly from -0.68 at $\alpha = 5°$ to -0.72 at $\alpha = 19°$. This could be due to the effect of

the shock, behind which the front boundary layer thickens as the angle of attack is increased. The sum C_{LV} of $C_{LV}(l)$ and $C_{LV}(w)$ is therefore negative, and decreases from -0.1 at $\alpha = 5°$ to a more negative value -0.36 at the higher $\alpha = 19°$, as noted above. Comparison of $C_{LR}(l)$ and $C_{LV}(l)$ indicates that the flow structures over the delta wing contribute more efficiently to $\hat{R}_e(\boldsymbol{x})$ than to $\hat{V}_e(\boldsymbol{x})$. Whilst C_{LV} is smaller than C_{LR} in magnitude, the value of $C_{LV}(w)$ is large and negative, and cancels a large part of the positive contributions from $C_{LV}(l)$, $C_{LR}(l)$ and perhaps $C_{LR}(w)$.

5.3.6. *Further discussion on $\hat{V}_e(\boldsymbol{x})$ and $\hat{R}_e(\boldsymbol{x})$-distributions*

In the above, we have examined the accumulated values of $\hat{R}_e(\boldsymbol{x})$ and $\hat{V}_e(\boldsymbol{x})$, integrated over either the whole flow field or the leeward and windward sides. It would also be interesting to learn how the source elements $\hat{R}_e(\boldsymbol{x})$ and $\hat{V}_e(\boldsymbol{x})$ are distributed in the flow field. Figure 13(*a*) shows contours of $\hat{V}_e(\boldsymbol{x})$, and figure 13(*b*) shows contours of $\hat{R}_e(\boldsymbol{x})$ for the case $M_\infty = 1.2$ and $\alpha = 19°$. It is observed that near the lower surface, the sign of $\hat{R}_e(\boldsymbol{x})$ is negative; this implies that the density along the lower surface of the delta wing is lower than the density just below it. For the same reason, the density along the upper surface is lower than the density just above it since the sign of $\hat{R}_e(\boldsymbol{x})$ is positive along the upper surface.

To understand the behaviour of $\hat{V}_e(\boldsymbol{x})$ and $\hat{R}_e(\boldsymbol{x})$, it is useful to consider that the flow consists of an infinite number of sections parallel to the cross-sections of the delta wing. The element $\hat{V}_e(\boldsymbol{x})$ must change its sign along a surface consisting of the centres of streamlines projected onto these planes. A centre of projected streamlines is typically a little away from the wall, and where the vorticity is roughly normal to the (projected) section passing through the centre, i.e. $\bar{\boldsymbol{\omega}} \approx \bar{\boldsymbol{\omega}}_p$. For the velocity, we write $\bar{\boldsymbol{u}} = \bar{\boldsymbol{u}}_p + \bar{\boldsymbol{u}}_n$, then the element $\bar{V}_e(\boldsymbol{x})$ (related to $\hat{V}_e(\boldsymbol{x})$ by (35)) is

$$-\bar{\rho}\bar{\boldsymbol{u}} \times \bar{\boldsymbol{\omega}} \cdot \nabla\phi = -\bar{\rho}\bar{\boldsymbol{u}}_n \times \bar{\boldsymbol{\omega}}_p \cdot \nabla\phi.$$

Near the centre, $\bar{\boldsymbol{u}}_n$ moves in a circle around the centre, and on the circle the vector $-\bar{\boldsymbol{u}}_n \times \bar{\boldsymbol{\omega}}_p$ is either always directed outward from the centre or toward it, and therefore must make a right angle twice with the smooth vector field $\nabla\phi$. This indicates that on each section, there is a dividing line of $\hat{V}_e(\boldsymbol{x})$, passing through the centre of the projected streamlines, and these dividing lines consist of a surface where the element $\hat{V}_e(\boldsymbol{x})$ changes its sign. From figure 13(*a*), it can be seen that the primary vortex is divided by one such line into a blue region of negative $\hat{V}_e(\boldsymbol{x})$ and a yellow region of positive $\hat{V}_e(\boldsymbol{x})$. Near the surface, the component $\bar{\boldsymbol{\omega}}_p$ changes its sign, and thus it is also seen that below the blue region there exists a red region of positive $\hat{V}_e(\boldsymbol{x})$.

Analogously $\hat{R}_e(\boldsymbol{x})$ or $\bar{R}_e(\boldsymbol{x}) = -\frac{1}{2}\bar{\boldsymbol{u}}^2\nabla\bar{\rho} \cdot \nabla\phi$ *must change its sign* along a surface passing through a line consisting of the points of maximum density; this can easily be understood by considering a cross-section. Notice that $\nabla\bar{\rho}$ either always points outward from, or toward the centre of density, while $\nabla\phi$ changes smoothly in its neighbourhood. If we move around the centre in a full circle, $\nabla\bar{\rho}$ must make a right angle twice with $\nabla\phi$; this therefore divides the core of density into two regions of opposite signs. For each cross-section, there are actually two centres of maximum density: one is that of the primary vortex and the other is associated with the secondary vortex. Refer to figure 13(*b*). The flow over the delta wing is therefore divided to four subregions of different signs of $\hat{R}_e(\boldsymbol{x})$: two positive and two negative. Next to the upper surface we have a region of positive sign, which consists of a layer inboard connected with the lower part of the secondary vortex. The upper part of the primary vortex is a region of positive $\hat{R}_e(\boldsymbol{x})$, which is connected to a quite large *region of strong expansion* around the leading edge. The region of expansion is positive

(*a*)

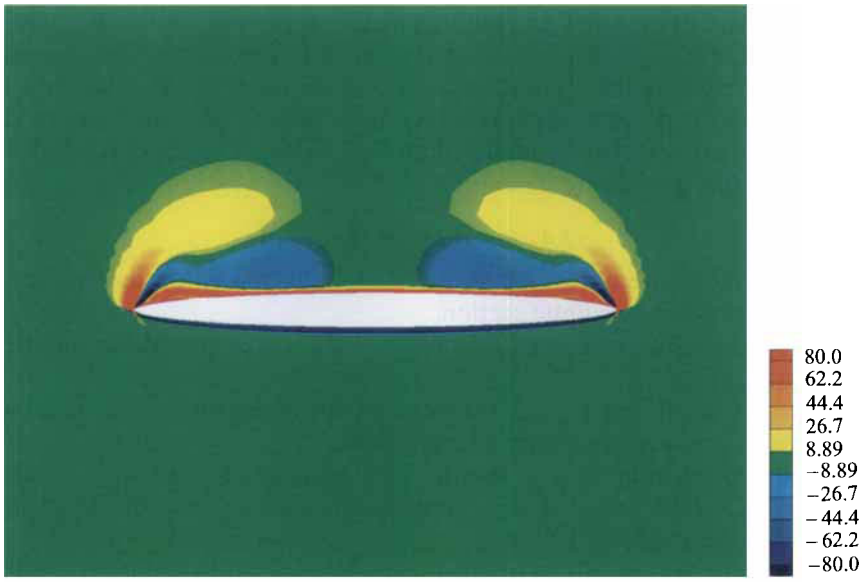

(*b*)

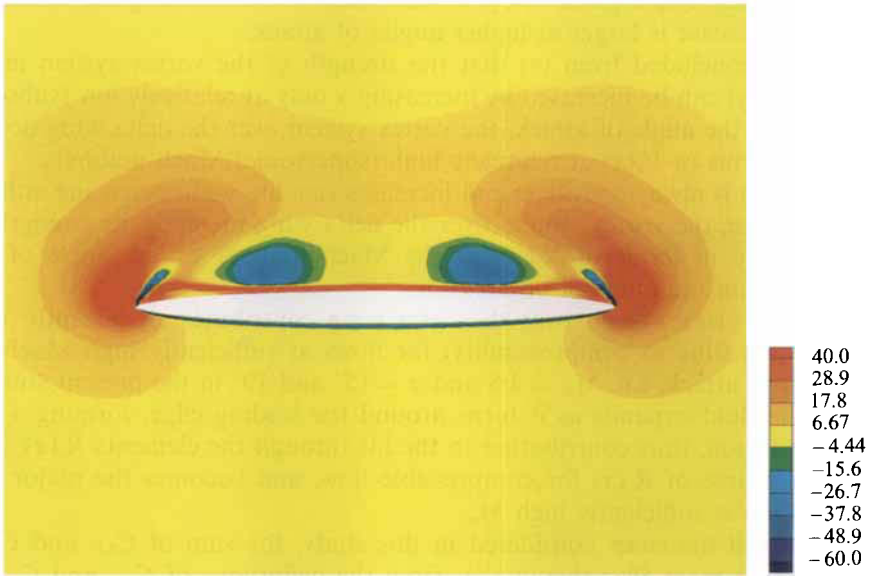

FIGURE 13. Contours of the source elements: (*a*) $\hat{V}_e(\boldsymbol{x}) = \bar{V}_e(\boldsymbol{x})/\frac{1}{2}M_\infty^2 S$ due to vorticity, (*b*) $\hat{R}_e(\boldsymbol{x}) = \bar{R}_e(\boldsymbol{x})/\frac{1}{2}M_\infty^2 S$ due to compressibility, at $M_\infty = 1.2$ and $\alpha = 19°$.

because around the leading edge the fluid expands and the density gradient $\nabla\bar{\rho}$ is therefore opposite to that of $\nabla\phi$, yielding positive $\bar{R}_e(\boldsymbol{x}) = -\frac{1}{2}\bar{\boldsymbol{u}}^2\nabla\bar{\rho}\cdot\nabla\phi$. The negative region lies in between, and consists of the inner lower part of the primary vortex and the upper part of the secondary vortex in terms of $\hat{R}_e(\boldsymbol{x})$. Roughly speaking, the major region of positive $\hat{R}_e(\boldsymbol{x})$ is larger than that of positive $\hat{V}_e(\boldsymbol{x})$ in size, while the region of negative $\hat{R}_e(\boldsymbol{x})$ is smaller than that of negative $\hat{V}_e(\boldsymbol{x})$ (though the scales shown are not the same in figure 13*a*, *b*).

5.4. *Summary of the results*

To summarize the above observations, we have found the following features for flows around the delta wing of elliptic section.

(i) The lift coefficient C_L (C_D) decreases with increasing Mach number M_∞, at the same angle of attack.

(ii) The lift coefficient C_L (C_D) increases with increasing angle of attack α; the rate of increase is slower at higher Mach number.

(iii) The contribution of C_{LV} due to $\hat{V}_e(\boldsymbol{x})$ dominates that of C_{LR} due to $\hat{R}_e(\boldsymbol{x})$ until $M_\infty = 0.75$. The value of C_{LV} even becomes *negative* as the Mach number is increased past about $M_\infty = 1.2$.

(iv) The contribution of $C_{LV}(w)$ is *always negative* and significant at all M_∞ and α values considered. The front boundary layer is a strong source of negative $\hat{V}_e(\boldsymbol{x})$, yielding negative $C_{LV}(w)$, whose magnitude decreases with increasing the angle of attack for $M_\infty = 0.6$, 0.8 and 1.2, but increases slightly at $M_\infty = 1.8$.

(v) $C_{LV}(l)$ behaves differently for subsonic $M_\infty = 0.6$, 0.8 and supersonic 1.2, 1.8. For the subsonic cases, $C_{LV}(l)$ increases with increasing α, whist decreasing for the supersonic cases. For a given α, $C_{LV}(l)$ decreases with increasing the Mach number; the rate of decrease is larger at higher angles of attack.

(vi) It is concluded from (v) that the strength of the vortex system in terms of $\hat{V}_e(\boldsymbol{x})$ (vorticity) can be increased by increasing α only at relatively low (subsonic) M_∞. By increasing the angle of attack, the vortex system over the delta wing decreases its strength in terms of $\hat{V}_e(\boldsymbol{x})$ at relatively high (supersonic) Mach numbers.

(vii) $C_{LR}(l)$ is always positive, and increases steadily with increasing either M_∞ or α. In this sense, the vortex system over the delta wing increases its strength through compressibility in terms of $\hat{R}_e(\boldsymbol{x})$, as the Mach number or the angle of attack is increased within the range of observations.

(viii) The vortex system over the delta wing contributes significantly to the lift through $\hat{R}_e(\boldsymbol{x})$ (due to compressibility) for flows at sufficiently high Mach numbers and angles of attack, e.g. $M_\infty = 1.8$ and $\alpha = 15°$ and 19° in the present study.

(ix) The fluid expands as it turns around the leading edge, forming a region of strong expansion, thus contributing to the lift through the elements $\hat{R}_e(\boldsymbol{x})$. This is an important source of $R_e(\boldsymbol{x})$ for compressible flow, and becomes the major source of positive $R_e(\boldsymbol{x})$ at sufficiently high M_∞.

(x) For all the cases considered in this study, the sum of C_{LV} and C_{LR} differs from C_L by at most 5%; this implies from the definitions of C_{LV} and C_{LR} that the wake region makes relatively small contribution to the lift coefficient C_L.

6. Concluding remarks

Flow control is one of the purposes in studying the aerodynamic forces, in particular, their relationships to flow structures. Efficient flow control relies on knowledge about the factors which may effect the change of flow (and thus the forces) as they vary in the

range of interest. In this regard, the present study provides a valuable examination of the aerodynamic forces by identifying two major sources $R_e(\boldsymbol{x})$ and $V_e(\boldsymbol{x})$, and gives a precise assessment of their relative importance in a range from high subsonic to supersonic flows over a delta wing. Vorticity has been naturally linked with the vortex system, and regarded as the major source of the lift for incompressible flows. From the present viewpoint, this is only partially true for subsonic flows, and is not at all correct for supersonic flows, especially at high Mach numbers. The region of density variation (and thus $\hat{R}_e(\boldsymbol{x})$) is not identical to the region of non-vanishing vorticity (and thus $\hat{V}_e(\boldsymbol{x})$); the importance of control of density variation for supersonic flights with the use of delta wings cannot be overestimated in favourable aerodynamic forces. Although the above analysis only concerns details for the lift coefficients, the analysis for the drag is very much the same and is not pursued further here.

The work is partially supported by the National Science Council of the Republic of China under Contracts NSC83-0401-E002-006 and NSC84-2212-E002-056. Free computing time on a CRAY-YMP/EL provided by the Computing Center of the Institute of Applied Mechanics is greatly acknowledged. The authors would like also to thank Dr Chi-Tzung Wang for his kind assistance in graphics, and are grateful to a reviewer who stimulated the writing of §4.1.

REFERENCES

BALDWIN, B. S. & LOMAX, H. 1978 Thin-layer approximation and algebraic model for separated turbulent flows. *AIAA Paper* 78-257.

CHANG, C. C. 1992 Potential flow and forces for incompressible viscous flow. *Proc. R. Soc. Lond.* A **437**, 517–525.

DEGANI, D. & SCHIFF, L. B. 1986 Computations of turbulent supersonic flows around pointed bodies having crossflow separation. *J. Comput. Phys.* **66**, 173–196.

GEE, K., CUMMINGS, R. M. & SCHIFF, L. B. 1992 Turbulence model effects on separated flow about a prolate spheroid. *AIAA J.* **30**, 655-664.

JAMESON, A. & YOON, S. 1987 Lower-upper implicit scheme with multiple grids for Euler equations. *AIAA J.* **25**, 929–935.

LAKSHMINARAYANA, B. 1986 Turbulence modeling for complex shear flows. *AIAA J.* **24**, 1900–1917.

LANDAU, L. D. & LIFSHITZ, E. M. 1987 *Fluid Mechanics* (2nd Edn). Pergamon Press.

LIGHTHILL, M. J. 1986 *An Informal Introduction to Theoretical Fluid Mechanics.* Oxford University Press.

MARVIN, J. G. 1983 Turbulence modeling for computational aerodynamics. *AIAA J.* **21**, 941–955.

MCMILLIN, S. N., PITTMAN, J. L. & THOMAS, J. L. 1990 A computational study of incipient leading-edge separation on a 65° delta wing at $M = 1.60$. *AIAA Paper* 90-3029-CP.

MILLER, D. S. & WOOD, R. M. 1983 An investigation of wing leading-edge vortices at supersonic speeds. *AIAA Paper* 83–1816.

NEWSOME, R. W. 1986 Euler and Navier-Stokes solutions for flow over a conical delta wing. *AIAA J.* **24**, 552–561.

PHILLIPS, O. M. 1956 The intensity of aeolian tones. *J. Fluid Mech.* **1**, 607–624.

SCHRADER, K. F., REYNOLDS G. A. & NOVAK, C. J. 1988 Effects of Mach number and Reynolds number on leading-edge vortices at high angle-of-attack. *AIAA Paper* 88-0172.

SQUIRE, L. C. 1985 Leading-edge separations and cross-flow shocks on delta wings. *AIAA J.* **23**, 321–325.

STANBROOK, A. & SQUIRE, L. C. 1964 Possible types of flow at swept leading edges. *Aero. Q.* **15**, 77–82.

VLADIMIROV, V. S. 1971 *Equations of Mathematical Physics.* Marcel Dekker.

WHITE, F. M. 1991 *Viscous Fluid Flow* (2nd Edn). McGraw-Hill.

WU, J. C. 1981 Theory for aerodynamic force and moment in viscous flows. *AIAA J.* **19**, 432–441.

YEE, H. C. & HARTEN, A. 1987 Implicit TVD schemes for hyperbolic conservation laws in curvilinear coordinates. *AIAA J.* **25**, 266–274.

YOKOTA, J. W. 1990 Diagonally inverted lower-upper factored implicit multigrid scheme for the three-dimensional Navier-Stokes equations. *AIAA J.* **28**, 1642–1649.